



Thermal and flow characterization in nanochannels with tunable surface wettability: A comprehensive molecular dynamics study

Haiyi Sun^{a†}, Zhike Liu^{a,b†}, Gongming Xin^c, Qian Xin^d, Jingzhi Zhang^c, Bing-Yang Cao^{b,c}, and Xinyu Wang^a

^aInstitute of Thermal Science and Technology, Shandong University, Jinan, P. R. China; ^bKey Laboratory for Thermal Science and Power Engineering of Ministry of Education, Department of Engineering Mechanics, Tsinghua University, Beijing, P. R. China; ^cSchool of Energy and Power Engineering, Shandong University, Jinan, P. R. China; ^dCenter of Nanoelectronics and School of Microelectronics, Shandong University, Jinan, P. R. China

ABSTRACT



The understanding of the convective heat transfer process for fluid flows through nanochannels becomes imperative due to the wide application of the micro/nanochannel cooling technology. In this work, thermal and flow characteristics in nanochannels with tunable surface wettability are investigated systematically using the molecular dynamics method. First, different temperature and velocity distributions in the entrance region and the fully developed region are observed in nanochannels at different surface wettabilities. The Kapitza resistance and boundary layer effect at the entrance induce the distinct temperature jump and velocity slip, which further determine the Nusselt number variation. Second, owing to the strengthening of the atom momentum exchange and wall shearing, the enhancement of the surface wettability boosts the convective heat transfer capacity and pressure drop in nanochannels. Meanwhile, we discover that a quasi-solid fluid layer appears near the wall when the wall-fluid interaction strength is strong enough and acts as a “phonon bridge” between the solid walls and the fluid to enhance the thermal energy transmission effectively. Finally, we evaluate the thermal and flow characteristics in nanochannels with tunable surface wettability comprehensively by the Colburn factor j and friction factor f and find out the optimum surface wettability range in nanochannels, corresponding to $\chi = 1.00$ – 1.75 .

ARTICLE HISTORY

Received 27 September 2019
Accepted 24 June 2020

1. Introduction

In the 1960s, Gordon Moore came up with a famous Moore’s Law which stated that the number of transistors on a microprocessor would double approximately every 18 months as well as their processing power would double accordingly [1]. However, the increasing power density, the high level of integration and the miniaturization are challenging the thermal management of these nanoelectronics, because the thermal issues may endanger the performance and life span of the devices potentially [2–4]. Hence, a number of methods are applied to improve the heat dissipation from these devices, such as phase-change cooling technology [5–8], jet cooling technology [9–11], micro/nanochannel cooling technology [12–15], and so on. Owing to the high heat

CONTACT Xinyu Wang  xyw@sdu.edu.cn  Institute of Thermal Science and Technology, Shandong University, 17923 Jingshi Road, Jinan, Shandong 250061 P. R. China.

[†]These authors contributed equally to this work.

transfer performance, compact structure and easy integration packaging, micro/nanochannel cooling technology stands out from the various heat dissipation strategies. In order to design the micro/nanochannel effectively, it is necessary to understand the thermal and flow characteristics in the micro/nanochannel comprehensively.

When the channel reaches the micro/nanoscale level, the thermal and flow characteristics of the fluid deviate from those at the macroscale, since the spatial scale of the channel becomes comparable to the mean free path of the fluid atoms [16–18]. A series of the experiments have been implemented to go into the differences between the convective heat transfer at the micro/nanoscale and macroscale. Knudstrup et al. observed the velocity slip in their experiments where hexane, dodecane, hexadecane and octamethylcyclotetrasiloxane were forced to flow through track-etched mica membranes with the size of about 30–300 Å [19]. Besides, by pumping the water in microchannels, Wu et al. investigated the laminar convective heat transfer and pressure drop in 13 different trapezoidal silicon microchannels and discovered the fluid temperature jump near the microchannel walls [20]. Furthermore, Wu et al. measured the friction factors when the gas conducted the laminar flow in the trapezoidal silicon microchannels and figured out that different surface roughness might result in the variation of the friction factors, which should be only decided by Reynolds numbers for the laminar flow at the macroscale [21]. By altering the surface roughness of the trapezoidal silicon microchannels, Qu et al. investigated on the pressure drop and heat transfer in the microchannels experimentally [13, 22]. Meanwhile, they established a roughness-viscosity model to analyze their experimental data and found that the Nusselt number decreased as the wall roughness increasing. When the scale decreases to the nanoscale ulteriorly, it seems that the experimental investigations of the thermal and flow characteristics in the nanochannels face enormous challenges. The molecular dynamics (MD) simulations about the flow in the nanochannels became popular since they are accomplished as long as the interatomic potential is definite. Ge et al. performed a molecular dynamics simulation on the convective heat transfer in nanochannels and they also captured the phenomena of the velocity slip and the temperature jump at the walls [23]. In addition, they calculated the local Nusselt number along the flow direction and figured out that the Nusselt number of the convective heat transfer in nanochannels was smaller than that at the macroscale due to the temperature jump near the nanochannel walls. By utilizing the MD simulations to calculate Peclet numbers (Pe), Gu et al. explored the effects of the axial heat conduction and viscous dissipation in the nanochannels [24]. The results pointed out that the contribution of the axial heat conduction and viscous dissipation to the fluid temperature development could be more than 33.2% when $Pe < 1$, which demonstrated that the axial heat conduction and viscous dissipation at the nanoscale for the low Pe played a significant role. Furthermore, with the implement of the MD simulations, Marable et al. focused on the advection heat flux at the nanoscale which was irrespective at the macroscale and uncovered that the advection heat flux was less than one tenth of the local surface flux [25]. However, the above experiments and simulations only focus on the thermal and flow characteristics at the thermal and hydraulic fully developed region. Therefore, the investigations of the thermal and flow performance at the thermal and hydraulic entrance region are inadequate, which is necessary for the further study.

On the other hand, numerous surface modification techniques are put forward to enhance the convective heat transfer in the micro/nanochannels, including tuning the surface wettability, creating the surface roughness, and adding the coating layers. Ge et al. investigated the Nusselt number variation when the surface wettability enhanced at the nanoscale and reported that the convective heat transfer in the nanochannel could be boosted by increasing the surface wettability [23]. In addition, by using the MD simulation to perform the convective heat transfer process in the rough nanochannels with the uniform and random groove widths, Chakraborty et al. made a conclusion that the surface roughness could always enhance the convective heat transfer no matter whether the surface roughness was regular or not because the surface roughness increased the

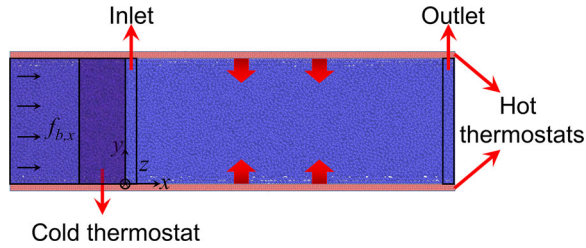


Figure 1. The schematic of the simulation domain.

heat transfer area between the fluid and wall [26]. Synchronously, they succeeded in improving the convective heat transfer in the nanochannel by adding the specific selected coating layers to the nanochannel surface. Besides, Marable et al. performed the non-equilibrium molecular dynamics simulations to study the thermal and flow performance when the water flowed in graphene nanochannels and the result showed that graphene was more suitable as the nanochannel material than silicon and aluminum [25]. Whereas, these studies just pay attention to the enhancement of the convective heat transfer blindly without considering the pressure drop and the energy consumption in the micro/nanochannel. In addition, the mechanism explanation of the convective heat transfer enhancement by modifying the nanochannel surface is also deficient. Hence, a comprehensive evaluation about thermal and flow characteristics is essential to the convective heat transfer in nanochannels.

Due to the prominent advantages of the molecular dynamics simulation in the study of the heat transfer at the nanoscale [27–31], we systematically investigate the thermal and flow characteristics in nanochannels with tunable surface wettability, using the non-equilibrium molecular dynamics simulation with the improved thermal pump method. First, we investigate the distributions of the temperature, velocity and pressure in nanochannels with different surface wettabilities, accompanying with the computations of the temperature slip length, velocity slip length and the local Nusselt number. Then momentum accommodation coefficients and phonon density of states (DOS) are adopted to explain the variation of the average Nusselt number with the increase of the wall-fluid interaction. Last, we evaluate the convective heat transfer performance in nanochannels with tunable surface wettability by the Colburn factor j and friction factor f , and find out the optimum range of the surface wettability under the consideration of the thermal and flow characteristics.

2. Simulation details

Figure 1 depicts the schematic of the simulation domain, in which two parallel walls construct the nanochannel and are composed of triple-layer copper atoms. Argon atoms, acting as the fluid, are confined between two copper walls. The two parallel copper walls possess the face-centered cubic (FCC) lattice structure and the lattice constant (a) is selected to be 3.615 \AA [32, 33]. Harmonic springs are employed to all copper atoms in order to connect copper atoms to FCC (100) lattice sites, which can well simulate the simple harmonic vibration of the copper atoms at the same frequency [23]. According to the Lindemann criterion [34, 35], the spring constant of all harmonic springs is set as $k=70 \text{ N/m}$ [23]. In our work, the size of all nanochannels is uniformly set to be $110a \times 30a \times 30a \text{ \AA}^3$, where the lattice constant of the copper a is taken as the unit size. In addition, it should be noted that the locations of two inner surfaces of copper walls are at $y=0 \text{ \AA}$ and $y=30a \text{ \AA}$, respectively. The whole copper walls contain 39600 copper atoms, and 83760 argon atoms are randomly distributed between two parallel walls. Based on the above channel volume and argon atom number, the corresponding average fluid density is about 1.2 g/cm^3 , which resembles the previous work [23].

All simulations in this work are implemented through the Large-scale Atomic/Molecular Massively Parallel Simulator (LAMMPS) package. In order to improve computational efficiency without affecting accuracy, only the attraction and repulsion forces are applied to describe the interatomic interactions, which are modeled as the 12-6 Lennard–Jones (L–J) potential:

$$U(r) = 4\varepsilon \left[\left(\frac{\sigma}{r} \right)^{12} - \left(\frac{\sigma}{r} \right)^6 \right] \quad (1)$$

where ε is the energy parameter, r is the interatomic distance and σ is the length parameter. To describe the argon–argon interaction, σ_{Ar-Ar} is set to be 3.405 Å and ε_{Ar-Ar} is equal to 0.0104 eV [36]. In addition, $\sigma_{Cu-Cu} = 2.338$ Å and $\varepsilon_{Cu-Cu} = 0.410$ eV are used for the Cu–Cu interaction in two solid walls [37]. The interaction parameters between argon atoms and copper atoms are as follows: $\sigma_{Ar-Cu} = 2.871$ Å and $\varepsilon_{Ar-Cu} = 0.065$ eV, which can be obtained by the Lorentz–Berthelot mixing rule [38]. In order to represent different surface wettabilities, we use a scaling parameter χ to tune the interfacial coupling strength between the fluid and walls. Here eight different scaling parameters are selected: $\chi = 0.25, 0.50, 0.75, 1.00, 1.25, 1.50, 1.75, 2.00$. The actual energy parameters between the copper atoms and argon atoms are the product of their intrinsic energy parameters and the scaling parameter. With the aim of improving the computational efficiency, the cutoff radius r_{cut} is set to be 10 Å and the atomic interactions beyond the cutoff radius are not taken into account [24].

To acquire the convective heat transfer performance between the nanochannel walls and fluid effectively, the thermal pump method is adopted in the simulation, which has been demonstrated to be able to describe the convective heat transfer well [23, 25, 26]. Using this method, the fluid domain is divided into three separate regions: a forcing region, a temperature reset region and a data collection region, which is shown in Figure 1. The forcing region locates in the range of $-10a$ Å $< x < -4a$ Å, where a constant body force $f_{b,x} = 1.7 \times 10^{-11}$ N is applied to the argon atoms to drive the advection flow. The temperature resetting is conducted only for the argon atoms inside the region of $-4a$ Å $< x < 0$ Å, where the thermal velocities of the fluid atoms are rescaled after removing the streaming velocity bias. When the argon atoms leave the temperature reset region, the streaming velocity which is removed for resetting temperature will be then added back to each argon atom to preserve the flow. After the argon atoms leave the temperature reset region, they enter into the data collection region where the convective heat transfer process is simulated. In this study, all fluid atoms flow from the entrance at a constant initial temperature T_{ini} and they exchange energy with two copper walls which maintain a fixed temperature T_w . Here we set T_{ini} and T_w as 200 K and 300 K, respectively. In an effort to increase the computational efficiency, the Verlet algorithm is employed to integrate Newton’s equations of motion within the simulation domain [39]. In addition, periodic boundary conditions are applied to the x and z directions, but non-periodic condition is for y direction. Under this simulation setup, our simulation can be on a par with the convective heat transfer process of fluid between two infinite plates at the macroscale.

All simulations are conducted for a total duration of 9.0 ns and the time step is chosen as 1.0 fs. The implementation details are as follows. First, each simulation spends 1 ns thermally relaxing the whole system in the NVT ensemble (constant number of atoms, volume, and temperature) in order to reach an initial equilibration condition. Subsequently, the system is switched to the NVE ensemble (constant number of atoms, volume, and energy), which lasts the next 8.0 ns. In the NVE process, a constant body force, $f_{b,x}$, is applied to all argon atoms in the forcing region. At the same time, both the wall temperature T_w and the fluid initial entrance temperature T_{ini} are controlled by the Langevin thermostats. We spend 2 ns in the NVE process to ensure the whole system to achieve a steady state. Afterwards, a lot of statistic in the data collection region, such as fluid temperature, velocity, and pressure, are recorded for 6 ns. Since the periodic boundary condition is applied in the flow direction, this setting induces the appearance of the unrealistic axial

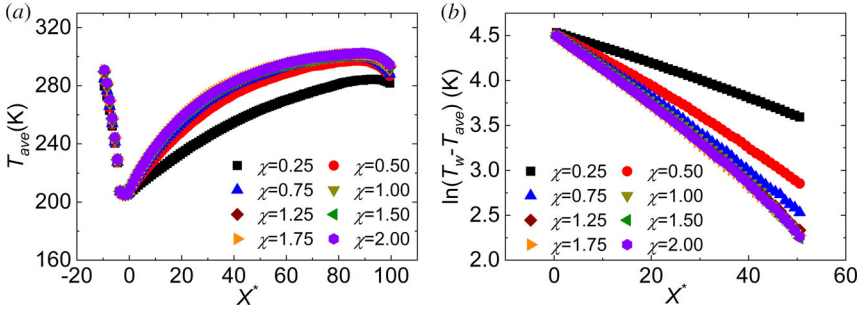


Figure 2. The variation of the average temperature (T_{ave}) along the flow direction (x direction) at different surface wettabilities.

heat conduction, which also exists in the preceding work [23, 24]. Hence, only the data from the first half of the data collection region are used for further analysis of the convection heat transfer, which refers to the range of $0 \text{ \AA} < x < 50a \text{ \AA}$. To describe the distribution of the temperature and velocity fields in each nanochannel, the nanochannel is divided into 110 columns along the x direction and 30 layers in the y direction. The size of each bin is $a \times a \times 30a \text{ \AA}^3$. To study the pressure development along the x direction, we calculate the pressure of the cross-section at an interval of $4a \text{ \AA}$ in the first half of the data collection region. In addition, an accurate and efficient algorithm for calculating the 3D pressure field is applied in this work simultaneously [40]. Meanwhile, we use the nondimensional parameters X^* and Y^* ($X^* = x/a$ and $Y^* = y/a$) to describe the position in the following section for the convenience.

3. Results and discussion

3.1. Thermal and flow characterization

To describe the temperature distribution, we first mathematically define the local average temperature, T_{ave} , in a specified cross-section along the flow direction as follows:

$$T_{ave}(x) = \frac{\int_0^H c\rho(x,y)v_f(x,y)T_f(x,y)dy}{\int_0^H c\rho(x,y)v_f(x,y)dy} \quad (2)$$

where H is the channel height, c is the specific heat capacity which is considered to be constant, $\rho(x,y)$ is the fluid density, $v_f(x,y)$ and $T_f(x,y)$ are the local fluid velocity and temperature. First of all, we study the local average temperature (T_{ave}) development along the x direction with different surface wettabilities, as shown in Figure 2. From Figure 2a, the local average temperatures, T_{ave} , decrease in the forcing region and are reset to the designated entrance temperature in all cases with different surface wettabilities, which agrees with the previous work [25]. In the data collection region, the T_{ave} rises along the flow direction firstly because the fluid atoms are heated by the walls with the constant temperature. However, the fluid temperatures near the outlet decrease unrealistically due to the unrealistic axial heat conduction. This unrealistic axial heat conduction is caused by the periodic boundary condition, which makes the outlet fluid temperature affected by the image atoms of the inlet cold fluid. Therefore, similar to the previous study [23], we just focus on the temperature distributions in the first half of the data collecting region. As depicted in Figure 2b, we also calculate the variation of the temperature difference between the fluid and walls along the flow direction. In general, the temperature difference between the fluid and walls shows the exponential decreasing trend along the flow direction for the convective heat transfer at the macroscale if the wall temperature is fixed. From Figure 2b, it can be observed that the temperature differences in all cases also reduce exponentially along the x direction, which is consistent with that at the macroscale. In order to portray the further details of the temperature

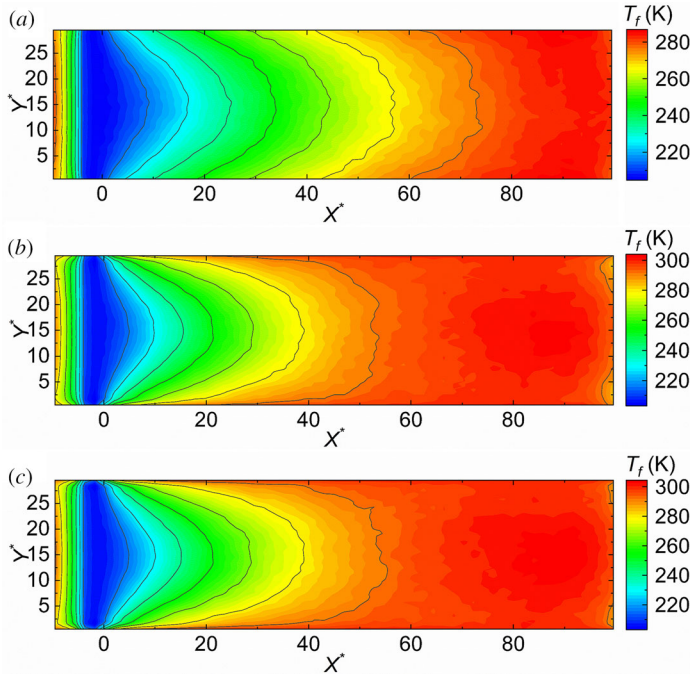


Figure 3. The temperature distributions along the flow direction (x direction) at (a) $\chi = 0.25$, (b) $\chi = 1.00$, and (c) $\chi = 2.00$.

distribution in x - y plane, **Figure 3** exhibits the fluid temperature distributions in nanochannels with three representative surface wettabilities ($\chi = 0.25, 1.00$ and 2.00), which refer to weak, normal and strong interfacial wettabilities. From three temperature distributions, we can find that the fluid is heated to higher temperature when it flows through the same channel length for larger χ , which indicates that the intensity of convective heat transfer is stronger in the channel with more wettable surface. Concurrently, we also choose the same parameters ($\chi = 0.25, 1.00$ and 2.00) to display the distribution of the fluid temperature (T_f) along the channel height (y direction) at different channel length positions in **Figure 4a-c**. The fluid temperature profile at $X^* = 0.5$ possesses a flattened middle region, while the profiles at the other positions appear parabolic trends. Such phenomena are in accordance with the thermal development law from the thermal entrance region to the fully thermal developed region at the macroscale. Additionally, we also observe that the difference between the mainstream temperature and the fluid temperature near the wall becomes larger when the wettability of the channel surface increases. The temperature jump between the wall and fluid near the wall can be observed obviously when the wall-fluid interaction strength is weak ($\chi = 0.25$), but such a phenomenon is no longer apparent when the wall-fluid interaction strength is strong enough ($\chi = 1.00$ or 2.00). To describe the relation between the temperature jump at the interface with the Kapitza resistance, R_{Kap} , we define the thermal slip length, l_k , to describe the fluid thermal behavior:

$$l_k = k_f R_{Kap} = \frac{T_w - T_f(x, y)|_{y=0}}{\left(\frac{\partial T_f(x, y)}{\partial y}\right)|_{y=0}} \quad (3)$$

where l_k is the thermal slip length, k_f is the thermal conductivity of the fluid, R_{Kap} is the Kapitza resistance, T_w is the wall temperature which is 300 K, $T_f(x, y)|_{y=0}$ is the near-wall fluid temperature and $(\partial T_f(x, y)/\partial y)|_{y=0}$ is the fluid temperature gradient at the wall. It must be noted that a quartic polynomial function is adopted to extrapolate the fluid temperature to determine both the $T_f(x, y)|_{y=0}$ and $(\partial T_f(x, y)/\partial y)|_{y=0}$. **Figure 5** shows the development of the thermal slip lengths

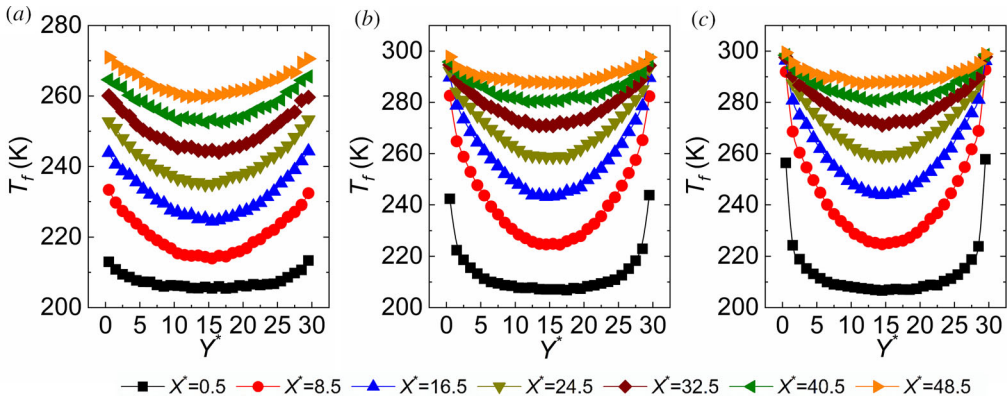


Figure 4. The fluid temperature profiles along the channel height (y direction) at different channel length positions at (a) $\chi = 0.25$, (b) $\chi = 1.00$, and (c) $\chi = 2.00$.

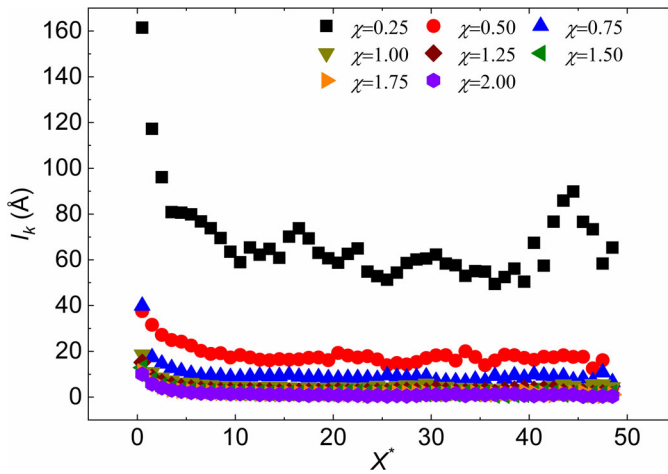


Figure 5. The variation of the thermal slip length along the flow direction (x direction) at different surface wettabilities.

along the x direction for different χ . As we can see from [Figure 5](#), the thermal slip lengths, corresponding to each χ , have the same change tendency along the flow direction. All of the thermal slip lengths decrease and gradually tend to be stable as a result of the fully thermal development. Furthermore, the smaller energy parameter, especially $\chi = 0.25$, gives rise to the larger thermal slip length, but the declining scope of the thermal slip length becomes smaller with the increase of the energy parameter. According to [Eq. \(3\)](#), the thermal slip length l_k is proportional to the Kapitza resistance at the wall-fluid interface, and thus the thermal slip length variation in [Figure 5](#) points out that the more hydrophilic surface possesses the smaller interfacial thermal resistance which promotes the heat transfer across the wall and fluid. Meanwhile, R_{Kap} at the entrance are always bigger than the steady value for all cases because the fluid fails to reach the stage of the fully thermal development.

Apart from the temperature field, the velocity distribution is also an important indicator to reflect the flow behavior in convective heat transfer. Parallel to the above temperature analysis, the same three scaling factors χ mentioned above are also selected to study the velocity distribution. [Figure 6](#) exhibits the velocity distributions along the channel height (y direction) at different channel length positions. The minimum and maximum velocity of the mainstream fluid is about 45 m/s and 80 m/s respectively, which fall into a reasonable velocity range as mentioned in the preceding study [[23](#), [41](#)]. We also confirm Reynolds numbers vary from 9.5 to 9.9, which proves

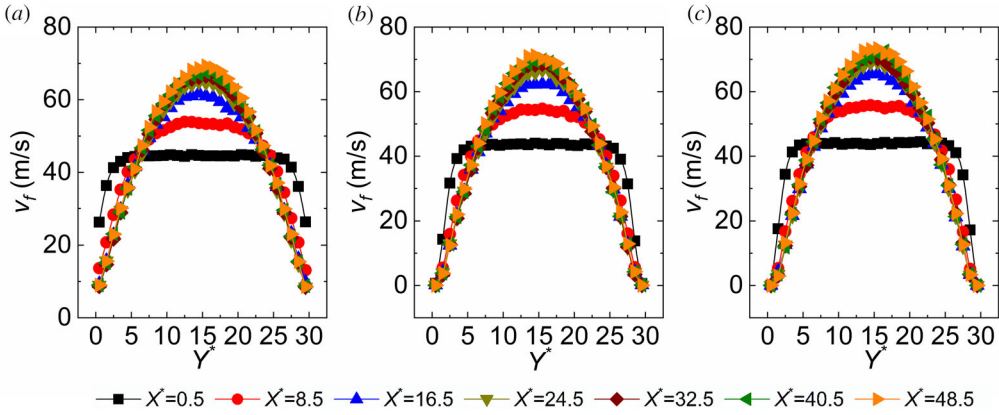


Figure 6. The fluid velocity profiles along the channel height (y direction) at different channel length positions at (a) $\chi = 0.25$, (b) $\chi = 1.00$, and (c) $\chi = 2.00$.

that the flow in our simulation is the laminar flow. We can see that the velocity slip can be evident at the interface when the wall-fluid interaction strength is weak ($\chi = 0.25$), whereas such phenomenon becomes inconspicuous when χ is 1.00 or 2.00. It can also be figured out that the velocity development in nanochannels can be divided into two regions in all three cases: the hydraulic entrance region and the fully hydraulic developed region, which analogizes the fluid flow at the macroscale. Figure 7 shows the schematics of the velocity development in the channels at the nanoscale and macroscale. Even though the velocity profile is comparable at the nanoscale and macroscale, due to the existence of the velocity slip, the velocity profile at the nanoscale is flatter than that at the macroscale, which means that the disparity between the near-wall fluid velocity and the mainstream fluid velocity is smaller in the nanochannel. Analogous to the temperature jump, the velocity slip can also be judged through the velocity slip length, l_s , which is identified as:

$$l_s = \frac{v_f(x, y)|_{y=0} - v_w}{\left(\frac{\partial v_f(x, y)}{\partial y}\right)|_{y=0}} \quad (4)$$

where l_s is the velocity slip length, $v_f(x, y)|_{y=0}$ is the near-wall fluid velocity, v_w is the wall velocity ($v_w = 0$ m/s), and $(\partial v_f(x, y)/\partial y)|_{y=0}$ is the velocity gradient of the fluid at the walls. We also use a quartic polynomial function to extrapolate the velocity profile to obtain both $v_f(x, y)|_{y=0}$ and $(\partial v_f(x, y)/\partial y)|_{y=0}$. For the same energy parameter χ , the velocity slip length of the hydraulic entrance region is always larger than that of the fully hydraulic developed region. In the fully hydraulic developed region, l_s maintains a stable value. With the surface wettability enhancing, l_k decreases and a negative l_k appears as shown in Figure 8. This boundary condition can be named as the negative slip condition [42].

On the other hand, we further characterize the pressure development along the flow direction and the result is shown in Figure 9. It can be noticed that the stronger surface wettability leads to the higher pressure at the same position, which is ascribed to the more drastic atom vibrations [43]. Moreover, the pressure development along the flow direction displays a little difference with the surface wettability of nanochannel enhanced. The pressure decreases linearly along the flow direction when the wall-fluid interaction is weak. However, when the energy parameter is large enough ($\chi > 1.00$), the pressure drop gradient in the hydraulic entrance region is different with that in the fully hydraulic developed region. The pressure drop speed at the entrance region is faster than that at the fully hydraulic developed region, which consists with the pressure development along the flow direction at the macroscale. Due to the growing of viscous boundary layers

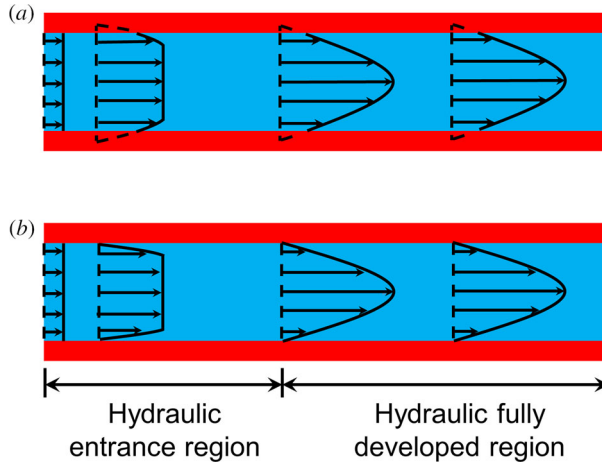


Figure 7. The schematics of the velocity development in the channels at the (a) nanoscale and (b) macroscale.

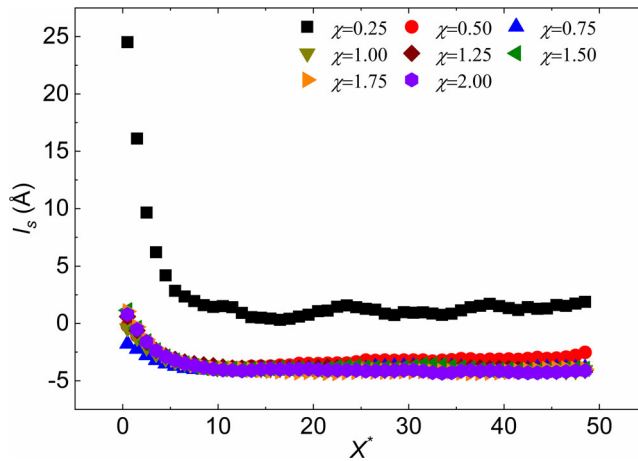


Figure 8. The variation of the velocity slip length along the flow direction (x direction) at different surface wettabilities.

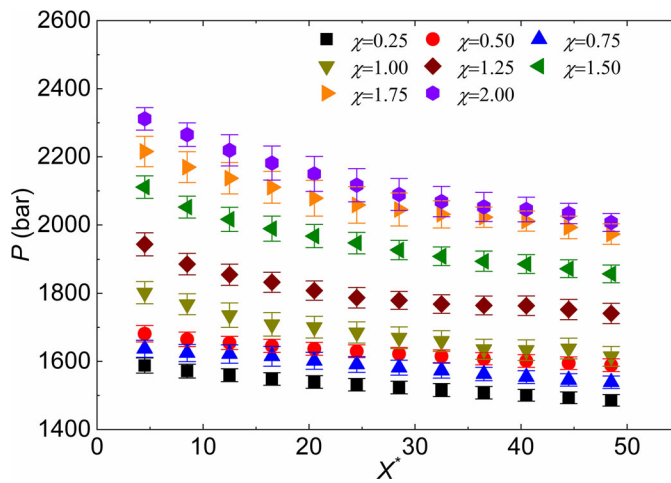


Figure 9. The variation of the pressure along the flow direction (x direction) at different surface wettabilities.

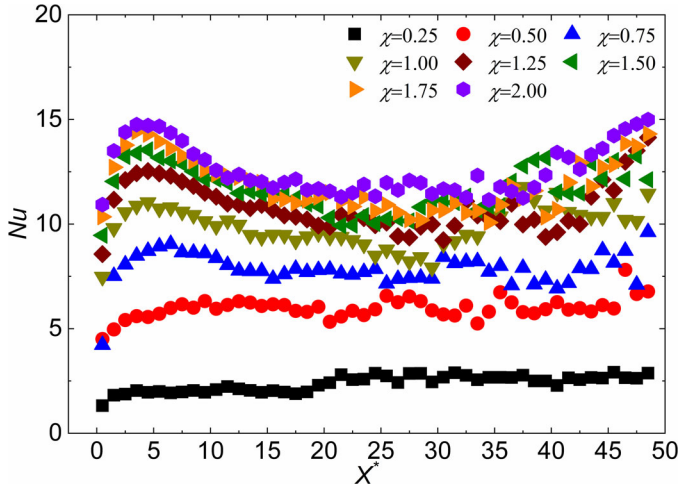


Figure 10. The variation of the local Nusselt number along the flow direction (x direction) at different surface wettabilities.

in the entrance region, the wall shearing in the flow developing region is larger than that in the fully hydraulic developed region, which generates the nonlinear pressure variation at the entrance region for larger χ .

For sake of evaluating the convective heat transfer capability along the flow direction, we calculate the local non-dimensional Nusselt number, Nu . The detailed derivations are as follows:

$$h(x) = \frac{q_{w/f}(x)}{T_w - T_{ave}(x)} \tag{5}$$

where $h(x)$ is the local heat transfer coefficient, $q_{w/f}(x)$ is the local heat flux across the channel surface. Generally, the local heat flux across the channel surface can be replaced by the local conduction heat flux ($q_c(x)$) among the fluid atoms at the macroscale since the no-slip boundary condition. However, the velocity slip may give rise to the surface advection flow and the temperature jump leads to the existence of the temperature difference between the fluid and wall. Therefore, the local advection heat flux ($q_a(x)$) exists in the nanochannels. Besides, the local viscous heat flux of the fluid ($q_v(x)$) would also be noteworthy due to the high surface-to-volume ratio in the nanochannels. Marable et al. have proved that the local advection heat flux is at least one order of magnitude smaller than the local heat flux across the nanochannel surface [25]. Furthermore, another work conducted by Gu et al. showed that the contribution of viscous dissipation to the heat flux could be below 2% when Peclet number ($Pe = Re \cdot Pr$) is larger than 10 [24]. By calculating Re and Prandtl number (Pr), all Peclet numbers in our simulation are approximately 10. Therefore, after neglecting the effects of the local surface advection flow and viscous dissipation, $q_{w/f}(x)$ can be equivalent to the local conduction heat flux among the fluid atoms in the y direction and calculated as follows:

$$q_{w/f}(x) = -k_f \frac{\partial T_f(x, y)}{\partial y} \Big|_{y=0} \tag{6}$$

By combining Eqs. (5)–(6), the local heat transfer coefficient, $h(x)$, and Nu are calculated as:

$$h(x) = \frac{k_f}{T_w - T_{ave}(x)} \frac{\partial T_f(x, y)}{\partial y} \Big|_{y=0} \tag{7}$$

and

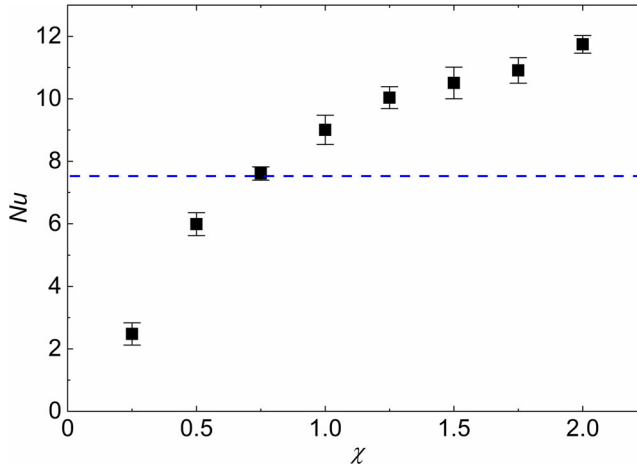


Figure 11. The variation of the average Nusselt number at different surface wettabilities. The dashed line represents the Nusselt number for the laminar flow between two parallel plates at the macroscale.

$$Nu = \frac{hD_c}{k_f} = \frac{2H}{T_w - T_{ave}(x)} \left. \frac{\partial T_f(x, y)}{\partial y} \right|_{y=0} \quad (8)$$

where D_c is the characteristic size which is set as $2H$. Figure 10 shows the variation of the local Nusselt number calculated with Eq. (8) along the flow direction corresponding to the different surface wetting conditions. The local Nusselt numbers at the entrance region are influenced by Kapitza resistance and boundary layer effect and show a diverse variation for different χ . When the wall-fluid interaction strength is weak, because of the impacts of the greater Kapitza resistance and the weak boundary layer effect, the local Nusselt numbers at the entrance are smaller than those at the fully hydraulic and thermal developed region. However, when χ becomes larger and the influence of the boundary layer gets intensified, the local Nusselt number increases first and then decreases until it gets stable. Different from the local Nu development in entrance region at the macroscale, the Kapitza resistance at the nanoscale cannot be neglected, which leads to the increase of Nu at the beginning of the entrance region. It needs to mention that the Nusselt number at $X^* > 35$ for larger χ increases mildly, which is ascribed to the effect of the viscous dissipation. Simultaneously, the local Nusselt number will boost with the enhancement of the wall-fluid interaction strength, but the improvement of the convective heat transfer becomes slighter when the surface wettability is very larger.

In a nutshell, the thermal and flow performances in the nanochannels show some differences from those at the macroscale, such as, the temperature jump and velocity slip. Different surface wettabilities and convective heat transfer development stages also leads to diverse temperature jumps and velocity slips. Especially, when the wall-fluid interaction strength is weak, the thermal slip length and the velocity slip length can be 161.4 \AA and 24.5 \AA at the entrance of the nanochannels, respectively. According to the above analysis, we can conclude that the characterization of both the velocity distribution and the pressure development at the nanoscale are similar to those at the macroscale when the surfaces are sufficiently hydrophilic. Additionally, it also needs to point out that enhancing surface wettability not only improves the convective heat transfer, but also increases the pressure in nanochannels.

3.2. Comprehensive evaluation of convection heat transfer

In order to directly compare the whole convective heat transfer capability in nanochannels at different surface wettabilities, we calculate the average Nusselt number in a designated thermal and

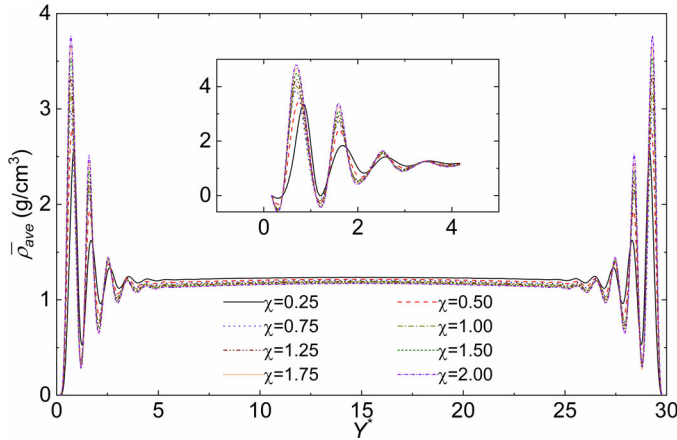


Figure 12. The average density profiles along the channel height (y direction) at different surface wettabilities. The inset is a zoom-in image of density at the near-wall region.

hydraulic developed region to conduct a comprehensive evaluation. This designated evaluation region is judged by Eqs. (9)–(10):

$$\frac{\partial}{\partial x} \left[\frac{T_w - T_f(x, y)}{T_w - T_{ave}(x)} \right] \approx 0 \quad (9)$$

$$\frac{\partial v_f(x, y)}{\partial x} \approx 0 \quad (10)$$

where $T_{ave}(x)$ is calculated by Eq. (2). By using Eqs. (9)–(10), the region of $16.5a \text{ \AA} < x < 28.5a \text{ \AA}$ is selected as the evaluation region of the convection heat transfer.

Figure 11 shows the arithmetic average values of the Nusselt number in the evaluation area. When the surface wettability enhances, the average Nu will increase from 2.48 to 11.74 while the increase rate will slow down. Generally, the fully developed Nusselt number for the laminar flow between two parallel plates with the constant wall temperature is 7.54 at the macroscale, which is corresponding to the Nu value for $\chi=0.75$ at the nanoscale. From Figure 11, we find that the average Nu for $\chi < 0.75$ is lower than that at the macroscale, which is attributed to the temperature jump at the interface in the nanochannel. However, when $\chi > 0.75$, the average Nu is higher than that of macroscale, which manifests that the strong surface wettability can make the convective heat transfer at the nanoscale surpass that at the macroscale.

To explain this enhancement for $\chi > 0.75$, we calculate the average fluid density along the channel height, the fluid velocity at the near-wall region, and the phonon DOS of the wall and fluid. At first, the average density distributions along the channel height (y direction) in the evaluation region at different surface wettabilities are calculated as shown in Figure 12. The density of the fluid atoms exhibits uneven layered and spatial fluctuation distributions near the solid wall. It is apparent that there are at least eight peaks of density near two walls and the distance between the adjacent layers is about the argon atom interaction distance (σ_{Ar-Ar}). In the density profiles, the first peak of the fluid density near the wall is the highest, which reflects the mean location of the first layer fluid atoms closest to the wall surface. This location is determined by the attraction and repulsion forces of the wall-fluid atoms. Besides, on account of the ordered arrangement of the wall atoms, the first layer of the fluid atoms comes into being a quasi-solid structure. Furthermore, when the fluid atoms are far away from the wall, due to the reduction of the interaction of the wall and fluid, the fluid density peak at other fluid atom layers will decline. It can also be seen from the density profiles that the first peak will move toward the wall when

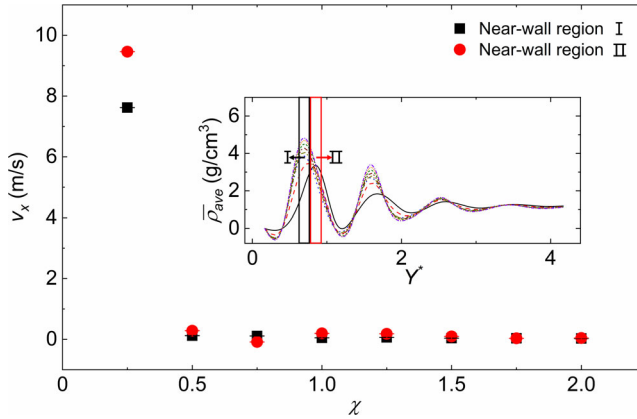


Figure 13. The variation of the near-wall fluid velocity at different surface wettabilities. The inset is used to distinguish two different near-wall regions.

the surface wettability increases, which verifies that the first layer fluid atoms are attracted close to the wall for the strong wall-fluid interaction [43]. In order to uncover the atomic layer movement near the wall, the fluid velocities of two near-wall regions with different wettabilities are recorded (Figure 13). When the wall-fluid interaction strength is weak ($\chi=0.25$), the average flow velocity of the fluid atoms near the wall is larger than 7 m/s, but when the wall-fluid interaction strength is strong, the average velocity of the fluid atoms near the wall is almost equal to zero which indicates that most of the fluid atoms near the walls are difficult to flow. We further monitor the trajectory of the fluid atoms near two walls for 0.2 ns to check the stability of the quasi-solid fluid layer near the walls when $\chi=0.25$ and $\chi=2.00$ (Figure 14). It shows that the quasi-solid fluid layers near the walls are unstable for $\chi=0.25$, which means that the near-wall fluid atoms exhibit fluid properties. However, the quasi-solid fluid layers near the walls resemble the solid for $\chi=2.00$. In a previous study, it has been proved that by adding the new material between the wall and fluid, the convective heat transfer capability would ascend significantly [26]. This new material acted as the “phonon bridge” to benefit the energy transport across wall-fluid interface. Also, we calculate the phonon DOS of the mainstream fluid, near-wall fluid, and solid walls for $\chi=0.25$ and $\chi=2.00$ to reveal phonon behaviors in the nanochannels (Figure 15). DOS can be calculated by taking the Fourier transform of the velocity autocorrelation function (VACF) [44–46]:

$$G(\omega) = \frac{1}{\sqrt{2\pi}} \int_{-\infty}^{+\infty} \frac{\langle v(0) \cdot v(t) \rangle}{\langle v(0) \cdot v(0) \rangle} e^{-i\omega t} dt \quad (11)$$

where v is the atomic velocity, and the angle brackets denote the ensemble averaging. As shown in Figure 15a, the DOS of the near-wall fluid is similar to that of the mainstream fluid for $\chi=0.25$, and the DOS of the fluid and wall show a smaller overlapping area. However, for $\chi=2$, the DOS peak of the near-wall fluid moves to that of the wall, which manifests that the near-wall fluid shows a quasi-solid behavior. Meanwhile, the DOS of the near-wall fluid for $\chi=2$ has the large overlapping areas with both the mainstream fluid and wall. To quantitatively assess the degree of the phonon vibration matching at the interface, we calculate the overlapping factor (S) by the follow equation [44, 47, 48]:

$$S = \frac{\int_{-\infty}^{+\infty} F_1(\omega) \cdot F_2(\omega) d\omega}{\int_{-\infty}^{+\infty} F_1(\omega) d\omega \int_{-\infty}^{+\infty} F_2(\omega) d\omega} \quad (12)$$

where subscripts “1” and “2” represent different materials. Table 1 displays the calculation results, where S_1 is the overlapping factor of the wall and near-wall fluid and S_2 is the overlapping factor

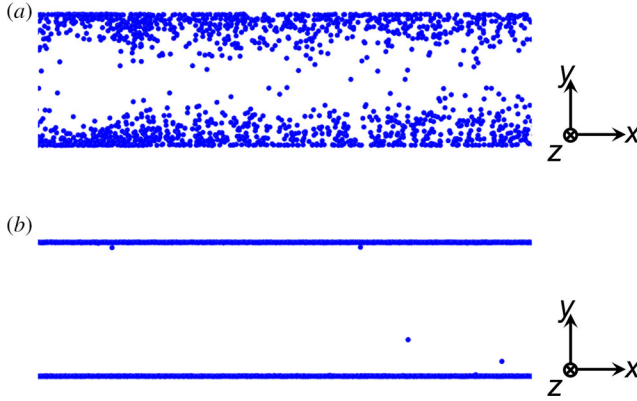


Figure 14. The trajectory of the quasi-solid fluid atoms at (a) $\chi = 0.25$ and (b) $\chi = 2.00$.

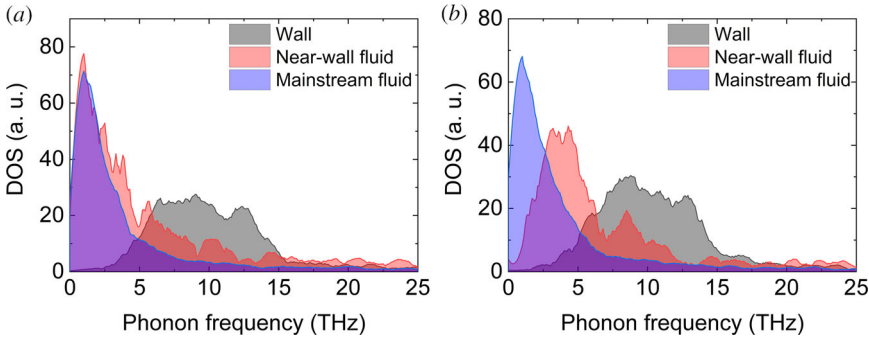


Figure 15. The phonon density of states of the wall, near-wall fluid, and mainstream fluid at (a) $\chi = 0.25$ and (b) $\chi = 2.00$.

Table 1. The overlapping factor at different surface wettabilities.

χ	S_1	S_2	$ S_1 - S_2 $
0.25	0.025	0.094	0.069
2.00	0.033	0.059	0.026

of the near-wall fluid and mainstream fluid. As the previous work pointed out, if the DOS overlapping area between the interface material and other two materials are similar, the interface material can bridge the phonon transmission channel between other two materials [49]. In our work, the absolute difference between S_1 and S_2 is 0.069 for $\chi = 0.25$ and 0.026 for $\chi = 2$, respectively. Hence, the near-wall fluid for $\chi = 2$ acts as the “phonon bridge” to facilitate the interfacial thermal transport and enhance the Nusselt number.

Knetchtel and Pitts firstly proposed the tangential momentum accommodation coefficients (TMAC) and the normal momentum accommodation coefficients (NMAC) when they studied the flow of the free molecules [50]. Since then, the TMAC and NMAC are used to characterize the momentum exchange in the wall-fluid interface, which are widely applied in many boundary models in theoretical and numerical researches [50–53]. When their values approach to 1, they indicate that the momentum exchange is more sufficient in the normal or tangential direction. The TMAC (α_t) and NMAC (α_n) are commonly defined as:

$$\alpha_t = \frac{M_{ti} - M_{tr}}{M_{ti} - M_{tw}} \quad (13)$$

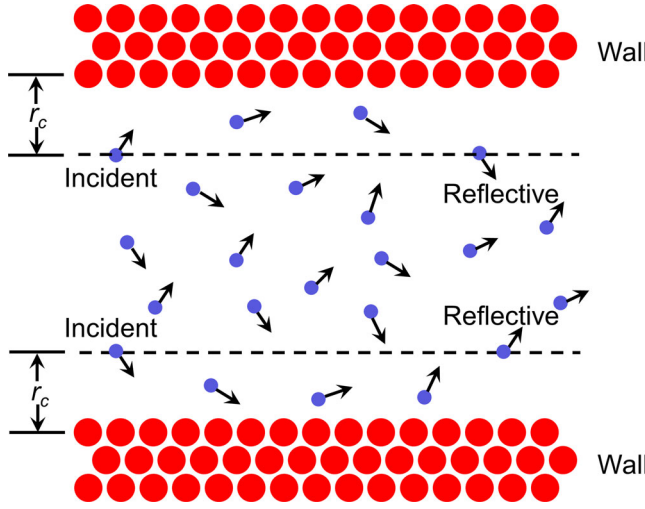


Figure 16. The schematic of the incidence-reflection process of the fluid atoms in the nanochannel.

$$\alpha_n = \frac{M_{ni} - M_{nr}}{M_{ni} - M_{nw}} \quad (14)$$

where M is the average momentum of fluid atoms, the subscripts “ t ” and “ n ” represent the tangential and normal components of the average momentum, and “ i ” and “ r ” represent the incident and reflected atoms. In the diffusive reflection, the fluid atoms are in equilibrium with the wall at a temperature T_w . The average tangential momentum (M_{tw}) and normal momentum (M_{nw}) for diffusively reflected atoms are expressed as:

$$M_{tw} = m_f v_w \quad (15)$$

$$M_{nw} = \sqrt{\pi m_f k_B T_w / 2} \quad (16)$$

where m_f is the fluid atom mass, v_w is the moving velocity of the wall and k_B is the Boltzmann constant. Since two walls are static ($v_w = 0$), M_{tw} is equal to zero. In Eqs. (13)–(16), since each momentum is a vector, the operation is also a vector operation.

Here, the accommodation coefficients for the fluid atoms and copper wall atoms are calculated according to a statistical algorithm using a three-dimensional molecular dynamics method to understand the atom collision and momentum exchange between the fluid atoms and solid walls. To calculate the accommodation coefficients, we firstly need to distinguish between the incident fluid atoms and reflected fluid atoms during the fluid-wall interactions. Figure 16 exhibits the schematic of the incidence-reflection process. We identify the incident fluid atoms and the reflected fluid atoms by their distances from the wall and the motion directions at the distance of cutoff radius from the wall [50]. In this work, more than 3 million momentum information of both the incident fluid atoms and reflected fluid atoms are obtained to calculate the accommodation coefficients by Eqs. (13)–(16). Figure 17 displays the variation of the accommodation coefficients for different wall-fluid interaction intensities. It can be observed that both TMAC and NMAC initially increase and then arrive at the plateau. With the increase of χ , the wall atoms bound the movement of the near-wall fluid atoms. The momentum exchange between the fluid atoms and walls is enhanced, which brings about the increase of TMAC and NMAC. The result can indirectly verify that the DOS overlapping area enhances for the larger surface wettability. Moreover, the coverage area of the adsorbed atoms is gradually enlarged, which makes the adsorbed atoms hinder the further momentum exchange between the fluid and walls. Therefore,

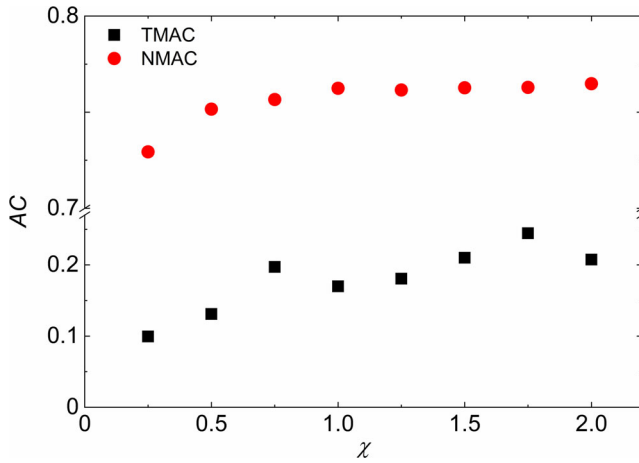


Figure 17. The variation of the momentum accommodation coefficients (TMAC and NMAC) at different surface wettabilities.

even though the wall-fluid interaction intensity continues to increase, the accommodation coefficients (TMAC and NMAC) cease the ulterior enhancement.

As discussed above, the momentum accommodation coefficients and the convective heat transfer cannot improve unlimitedly with increasing the parameter χ . Simultaneously, the χ enhancement will give rise to the pressure enlargement. The preceding work uncovered that the increase of the wall-fluid interaction would lead to the friction enhancement, which enlarged the pressure drop and energy consumption [54]. To obtain the optimum surface wettability, it is necessary to further perform a comprehensive evaluation of the convective heat transfer including thermal and flow characteristics in the nanochannel. To investigate into the mechanisms of the heat and mass transfer and evaluate the performance of the convective heat transfer comprehensively, Colburn and Chilton put forward the dimensionless factor j and the friction factor f [55, 56], which have been widely applied to evaluate the convective heat transfer process under the different applications [57–60]. Basing on the Colburn factor j and friction factor f , there are three comprehensive evaluation performance indicators: j/f , $j/f^{1/2}$ and $j/f^{1/3}$, which are suitable for the evaluation of the convective heat transfer under the conditions of equal flow rate, equal pressure drop and equal pump power, respectively. Here we use these two factors to assess the thermal and flow characteristics in nanochannels. The Colburn factor j and friction factor f are calculated as:

$$j = \frac{Nu}{Re \cdot Pr^{1/3}} \tag{17}$$

$$f = \frac{\Delta P}{1/2 \bar{\rho}_m \cdot \bar{v}_{ave}^2} \cdot \frac{D_c}{L} \tag{18}$$

where ΔP is the pressure difference between the inlet and outlet, and L is the length from the inlet to the outlet of the evaluation region ($X^* = 16.5$ for the inlet and $X^* = 28.5$ for the outlet), $\bar{\rho}_m$ is the average density of the evaluation region and \bar{v}_{ave} is the average velocity of the evaluation region. The average temperature \bar{T}_{ave} , average velocity \bar{v}_{ave} and average density $\bar{\rho}_{ave}$ of the evaluation region are obtained by the following formulas:

$$\bar{T}_{ave} = \frac{\int_{x_{in}}^{x_{out}} T_{ave}(x) dx}{x_{out} - x_{in}} \tag{19}$$

$$\bar{v}_{ave} = \frac{\int_{x_{in}}^{x_{out}} v_{ave}(x) dx}{x_{out} - x_{in}} \tag{20}$$

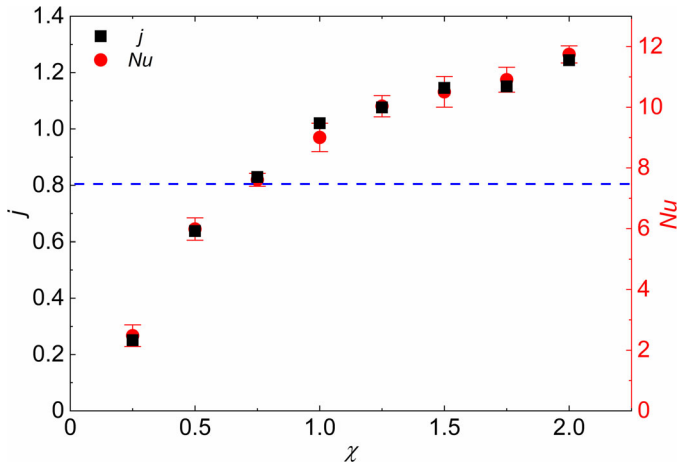


Figure 18. The variation of the Colburn factor j and the Nusselt number at different surface wettabilities. The dashed line represents the Nusselt number for the laminar flow between two parallel plates at the macroscale.

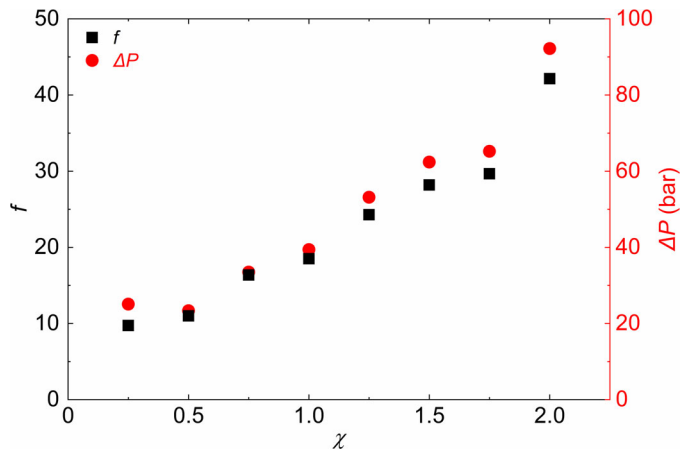


Figure 19. The variation of the friction factor f and pressure drop at different surface wettabilities.

$$\bar{\rho}_{ave} = \frac{\int_{x_{in}}^{x_{out}} \rho_{ave}(x) dx}{x_{out} - x_{in}} \quad (21)$$

where $x_{in} = 16.5a \text{ \AA}$ and $x_{out} = 28.5a \text{ \AA}$, corresponding to the inlet and outlet of the evaluation region, and $T_{ave}(x)$, $v_{ave}(x)$ and $\rho_{ave}(x)$ are the average temperature, velocity and density of the local cross-sections. $v_{ave}(x)$ and $\rho_{ave}(x)$ are evaluated as:

$$v_{ave}(x) = \frac{\int_0^H \rho(x, y) v_f(x, y) dy}{\int_0^H \rho(x, y) dy} \quad (22)$$

$$\rho_{ave}(x) = \frac{\int_0^H \rho(x, y) dy}{H} \quad (23)$$

All thermal physical properties are obtained from database of the National Institute of Standards and Technology under the average temperature of the evaluation region \bar{T}_{ave} .

As shown in **Figure 18**, the Colburn factor j increases with the surface wettability enhancing, which is in line with the Nusselt number variation. Similarly, the friction factors f and pressure

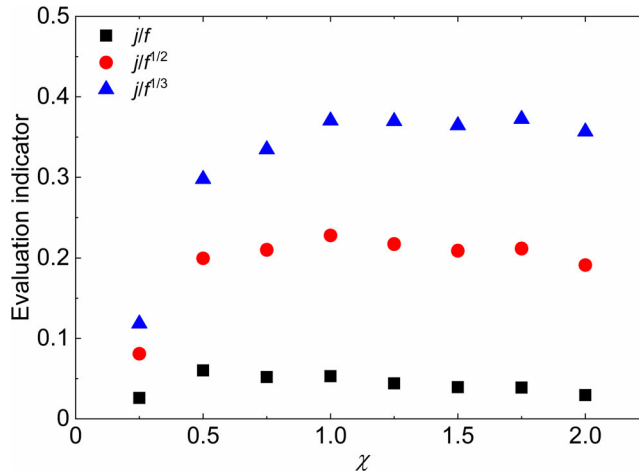


Figure 20. The variation of three comprehensive evaluation indicators at different surface wettabilities.

drop show the monotonic increasing trends at different χ , which are displayed in Figure 19. It can be seen from both Figures 18 and 19 that the Colburn factor j and friction factor f can reflect the heat transfer and pressure loss characteristics precisely. Figure 20 reveals the three evaluation indicators variation for convective heat transfer in the nanochannel with tunable surface wettability. It needs to be figured out that increasing surface wettability cannot always improve the comprehensive performance of the heat transfer and flow. The higher surface wettability will lead to excessive energy consumption. In our cases, $\chi=1.00\text{--}1.75$ is a favorable range to obtain the best convective heat transfer performance in the nanochannel.

4. Conclusions

In this work, thermal and flow characteristics in nanochannels with tunable surface wettability are investigated systematically using the molecular dynamics method. In comparison with the conventional channel flow at the macroscale, the temperature jump and velocity slip are observed at the wall-fluid interface. Due to the incomplete development of the velocity and temperature, the thermal slip and velocity slip lengths in the entrance region are larger than those in the fully developed region, which has remarkable influences on the heat transfer and flow. The local Nusselt number at the entrance is determined by both the Kapitza resistance and boundary layer effect, which differs from that at the macroscale. With the surface wettability enhancing, the convective heat transfer capability and pressure drop will be raised. Besides, the phonon density of states and the momentum accommodation coefficients are calculated to interpret the Nu enhancement. We find out that the quasi-solid fluid atoms induced by the higher surface wettability act as the “phonon bridge” to promote the thermal energy transmission between the fluid and the wall. Finally, due to the synchronous enhancement of Nu and pressure drop, we adopt the Colburn factor j and friction factor f to perform the comprehensive evaluation of the thermal and flow characteristics in nanochannels. The results demonstrate that $\chi=1.00\text{--}1.75$ is a favorable range to obtain the optimum convective heat transfer performance in nanochannels. Our work is expected to provide the fundamental knowledge about the thermal and flow characteristics in nanochannels to guide the thermal management of the micro/nanodevices.

Disclosure statement

There are no conflicts to declare.

Funding

This work was supported by the National Natural Science Foundation of China (No. 51806123), the Key R&D Program of Shandong Province, China (No. 2019GGX101030), the China Postdoctoral Science Foundation (No. 2018M642654), the Natural Science Foundation of Shandong Province, China (No. ZR2018BEE025, No. ZR2019MEE024), the Fundamental Research Funds for the Central Universities (No. 2018JC037), and the Fundamental Research Funds of Shandong University, China (No. 2018TB007).

References

- [1] R. R. Schaller, "Moore's law: Past, present and future," *IEEE Spectr.*, vol. 34, no. 6, pp. 52–59, 1997. DOI: [10.1109/6.591665](https://doi.org/10.1109/6.591665).
- [2] A. L. Moore and L. Shi, "Emerging challenges and materials for thermal management of electronics," *Mater. Today*, vol. 17, no. 4, pp. 163–174, 2014. DOI: [10.1016/j.mattod.2014.04.003](https://doi.org/10.1016/j.mattod.2014.04.003).
- [3] A. Kumar, S. Nath and D. Bhanja, "Effect of nanofluid on thermo hydraulic performance of double layer tapered microchannel heat sink used for electronic chip cooling," *Numer. Heat Transfer, Part A*, vol. 73, no. 7, pp. 429–445, 2018. DOI: [10.1080/10407782.2018.1448611](https://doi.org/10.1080/10407782.2018.1448611).
- [4] Q. Yao, T. M. Shih, R. R. G. Chang, Z. Chen, Y. L. Gao and Y. J. Lu, "Optimization of the cooling characteristics in high-voltage LEDs," *Numer. Heat Transfer, Part A*, vol. 69, no. 11, pp. 1242–1252, 2016. DOI: [10.1080/10407782.2015.1127727](https://doi.org/10.1080/10407782.2015.1127727).
- [5] M. Jaworski, "Thermal performance of heat spreader for electronics cooling with incorporated phase change material," *Appl. Therm. Eng.*, vol. 35, pp. 212–219, 2012. DOI: [10.1016/j.applthermaleng.2011.10.036](https://doi.org/10.1016/j.applthermaleng.2011.10.036).
- [6] H. Yin, X. Gao, J. Ding and Z. Zhang, "Experimental research on heat transfer mechanism of heat sink with composite phase change materials," *Energy Convers. Manage.*, vol. 49, no. 6, pp. 1740–1746, 2008. DOI: [10.1016/j.enconman.2007.10.022](https://doi.org/10.1016/j.enconman.2007.10.022).
- [7] C. Lian, Y. Wang, Q. Li, H. Li and X. He, "Numerical investigation on the performance of microencapsulated phase change material suspension applied to liquid cold plates," *Numer. Heat Transfer, Part A*, vol. 75, no. 5, pp. 342–358, 2019. DOI: [10.1080/10407782.2019.1595817](https://doi.org/10.1080/10407782.2019.1595817).
- [8] Q. Cao and Z. Cui, "Molecular dynamics simulations of the effect of surface wettability on nanoscale liquid film phase-change," *Numer. Heat Transfer, Part A*, vol. 75, no. 8, pp. 533–547, 2019. DOI: [10.1080/10407782.2019.1608768](https://doi.org/10.1080/10407782.2019.1608768).
- [9] X. Luo, S. Liu, X. Jiang and T. Cheng, "Experimental and numerical study on a micro jet cooling solution for high power LEDs," *Sci. China Ser. E*, vol. 50, no. 4, pp. 478–489, 2007. DOI: [10.1007/s11431-007-0028-y](https://doi.org/10.1007/s11431-007-0028-y).
- [10] S. G. Kandlikar and A. V. Bapat, "Evaluation of jet impingement, spray and microchannel chip cooling options for high heat flux removal," *Heat Transfer Eng.*, vol. 28, no. 11, pp. 911–923, 2007. DOI: [10.1080/01457630701421703](https://doi.org/10.1080/01457630701421703).
- [11] I. Zahmatkesh and S. A. Naghedifar, "Oscillatory mixed convection in the jet impingement cooling of a horizontal surface immersed in a nanofluid-saturated porous medium," *Numer. Heat Transfer, Part A*, vol. 72, no. 5, pp. 401–416, 2017. DOI: [10.1080/10407782.2017.1376961](https://doi.org/10.1080/10407782.2017.1376961).
- [12] E. Pop, "Energy dissipation and transport in nanoscale devices," *Nano Res*, vol. 3, no. 3, pp. 147–169, 2010. DOI: [10.1007/s12274-010-1019-z](https://doi.org/10.1007/s12274-010-1019-z).
- [13] W. Qu, G. M. Mala and D. Li, "Pressure-driven water flows in trapezoidal silicon microchannels," *Int. J. Heat Mass Transfer*, vol. 43, no. 3, pp. 353–364, 2000.
- [14] F. Ahmad, T. A. Cheema, M. M. Ur Rehman, A. Abbas and C. W. Park, "Thermal enhancement of microchannel heat sink using rib surface refinements," *Numer. Heat Transfer, Part A*, vol. 76, no. 11, pp. 851–870, 2019. DOI: [10.1080/10407782.2019.1673104](https://doi.org/10.1080/10407782.2019.1673104).
- [15] T. W. Kim and T. S. Park, "Size effect on compressible flow and heat transfer in microtube with rarefaction and viscous dissipation," *Numer. Heat Transfer, Part A*, vol. 76, no. 11, pp. 871–888, 2019. DOI: [10.1080/10407782.2019.1673106](https://doi.org/10.1080/10407782.2019.1673106).
- [16] B. Y. Cao, M. Chen and Z. Y. Guo, "Liquid flow in surface-nanostructured channels studied by molecular dynamics simulation," *Phys. Rev. E*, vol. 74, no. 6, pp. 066311, 2006. DOI: [10.1103/PhysRevE.74.066311](https://doi.org/10.1103/PhysRevE.74.066311).
- [17] L. Bocquet and J. L. Barrat, "Flow boundary conditions from nano-to micro-scales," *Soft Matter*, vol. 3, no. 6, pp. 685–693, 2007. DOI: [10.1039/b616490k](https://doi.org/10.1039/b616490k).
- [18] C. Zhang and Y. Chen, "Slip behavior of liquid flow in rough nanochannels," *Chem. Eng. Process*, vol. 85, pp. 203–208, 2014. DOI: [10.1016/j.cep.2014.09.003](https://doi.org/10.1016/j.cep.2014.09.003).
- [19] T. G. Knudstrup, I. A. Bitsanis and G. B. Westermann-Clark, "Pressure-driven flow experiments in molecularly narrow, straight pores of molecular dimension in mica," *Langmuir*, vol. 11, no. 3, pp. 893–897, 1995. DOI: [10.1021/la00003a036](https://doi.org/10.1021/la00003a036).

- [20] H. Y. Wu and P. Cheng, "An experimental study of convective heat transfer in silicon microchannels with different surface conditions," *Int. J. Heat Mass Transfer*, vol. 46, no. 14, pp. 2547–2556, 2003. DOI: [10.1016/S0017-9310\(03\)00035-8](https://doi.org/10.1016/S0017-9310(03)00035-8).
- [21] P. Wu and W. A. Little, "Measurement of friction factors for the flow of gases in very fine channels used for microminiature Joule-Thomson refrigerators," *Cryogenics*, vol. 23, no. 5, pp. 273–277, 1983. DOI: [10.1016/0011-2275\(83\)90150-9](https://doi.org/10.1016/0011-2275(83)90150-9).
- [22] W. Qu, G. M. Mala and D. Li, "Heat transfer for water flow in trapezoidal silicon microchannels," *Int. J. Heat Mass Transfer*, vol. 43, no. 21, pp. 3925–3936, 2000. DOI: [10.1016/S0017-9310\(00\)00045-4](https://doi.org/10.1016/S0017-9310(00)00045-4).
- [23] S. Ge, Y. Gu and M. Chen, "A molecular dynamics simulation on the convective heat transfer in nano-channels," *Mol. Phys.*, vol. 113, no. 7, pp. 703–710, 2015. DOI: [10.1080/00268976.2014.970593](https://doi.org/10.1080/00268976.2014.970593).
- [24] Y. W. Gu, S. Ge and M. Chen, "A molecular dynamics simulation of nanoscale convective heat transfer with the effect of axial heat conduction," *Mol. Phys.*, vol. 114, no. 12, pp. 1922–1930, 2016. DOI: [10.1080/00268976.2016.1168884](https://doi.org/10.1080/00268976.2016.1168884).
- [25] D. C. Marable, S. Shin and A. Y. Nobakht, "Investigation into the microscopic mechanisms influencing convective heat transfer of water flow in graphene nanochannels," *Int. J. Heat Mass Transfer*, vol. 109, pp. 28–39, 2017. DOI: [10.1016/j.ijheatmasstransfer.2017.01.100](https://doi.org/10.1016/j.ijheatmasstransfer.2017.01.100).
- [26] P. Chakraborty, T. Ma, L. Cao and Y. Wang, "Significantly enhanced convective heat transfer through surface modification in nanochannels," *Int. J. Heat Mass Transfer*, vol. 136, pp. 702–708, 2019. DOI: [10.1016/j.ijheatmasstransfer.2019.03.053](https://doi.org/10.1016/j.ijheatmasstransfer.2019.03.053).
- [27] H. Babaei, P. Keblinski and J. Khodadadi, "A proof for insignificant effect of Brownian motion-induced micro-convection on thermal conductivity of nanofluids by utilizing molecular dynamics simulations," *J. Appl. Phys.*, vol. 113, no. 8, pp. 084302, 2013. DOI: [10.1063/1.4791705](https://doi.org/10.1063/1.4791705).
- [28] W. Cui, Z. Shen, J. Yang and S. Wu, "Effect of chaotic movements of nanoparticles for nanofluid heat transfer augmentation by molecular dynamics simulation," *Appl. Therm. Eng.*, vol. 76, pp. 261–271, 2015. DOI: [10.1016/j.applthermaleng.2014.11.030](https://doi.org/10.1016/j.applthermaleng.2014.11.030).
- [29] A. Rajabpour, F. Y. Akizi, M. M. Heyhat and K. Gordiz, "Molecular dynamics simulation of the specific heat capacity of water-Cu nanofluids," *Int. Nano Lett.*, vol. 3, no. 1, pp. 58, 2013.
- [30] C. Hu, M. Bai, J. Lv and X. Li, "An investigation on the flow and heat transfer characteristics of nanofluids by nonequilibrium molecular dynamics simulations," *Numer. Heat Transfer, Part B*, vol. 70, no. 2, pp. 152–163, 2016. DOI: [10.1080/10407790.2016.1177398](https://doi.org/10.1080/10407790.2016.1177398).
- [31] X. Yin, C. Hu, M. Bai and J. Lv, "Molecular dynamics simulation on the effect of nanoparticles on the heat transfer characteristics of pool boiling," *Numer. Heat Transfer, Part B*, vol. 73, no. 2, pp. 94–105, 2018. DOI: [10.1080/10407790.2017.1420323](https://doi.org/10.1080/10407790.2017.1420323).
- [32] L. Li, P. Ji and Y. Zhang, "Molecular dynamics simulation of condensation on nanostructured surface in a confined space," *Appl. Phys. A*, vol. 122, no. 5, pp. 496, 2016. DOI: [10.1007/s00339-016-0032-9](https://doi.org/10.1007/s00339-016-0032-9).
- [33] Y. N. Osetsky, A. Serra, B. N. Singh and S. I. Golubov, "Structure and properties of clusters of self-interstitial atoms in fcc copper and bcc iron," *Philos. Mag. A*, vol. 80, no. 9, pp. 2131–2157, 2000. DOI: [10.1080/01418610050132747](https://doi.org/10.1080/01418610050132747).
- [34] N. V. Priezjev, "Effect of surface roughness on rate-dependent slip in simple fluids," *J. Chem. Phys.*, vol. 127, no. 14, pp. 144708, 2007. DOI: [10.1063/1.2796172](https://doi.org/10.1063/1.2796172).
- [35] S. Sarkar, C. Jana and B. Bagchi, "Breakdown of universal Lindemann criterion in the melting of Lennard-Jones polydisperse solids," *J. Chem. Sci.*, vol. 129, no. 7, pp. 833–840, 2017. DOI: [10.1007/s12039-017-1245-y](https://doi.org/10.1007/s12039-017-1245-y).
- [36] F. Müller-Plathe, "A simple nonequilibrium molecular dynamics method for calculating the thermal conductivity," *J. Chem. Phys.*, vol. 106, no. 14, pp. 6082–6085, 1997. DOI: [10.1063/1.473271](https://doi.org/10.1063/1.473271).
- [37] R. Wang, S. Qian and Z. Zhang, "Investigation of the aggregation morphology of nanoparticle on the thermal conductivity of nanofluid by molecular dynamics simulations," *Int. J. Heat Mass Transfer*, vol. 127, pp. 1138–1146, 2018. DOI: [10.1016/j.ijheatmasstransfer.2018.08.117](https://doi.org/10.1016/j.ijheatmasstransfer.2018.08.117).
- [38] C. L. Kong, "Combining rules for intermolecular potential parameters. II. Rules for the Lennard-Jones (12-6) potential and the Morse potential," *J. Chem. Phys.*, vol. 59, no. 5, pp. 2464–2467, 1973. DOI: [10.1063/1.1680358](https://doi.org/10.1063/1.1680358).
- [39] L. Verlet, "Computer "experiments" on classical fluids. I. Thermodynamical properties of Lennard-Jones molecules," *Phys. Rev.*, vol. 159, no. 1, pp. 98–103, 1967. DOI: [10.1103/PhysRev.159.98](https://doi.org/10.1103/PhysRev.159.98).
- [40] T. Nakamura, S. Kawamoto and W. Shinoda, "Precise calculation of the local pressure tensor in Cartesian and spherical coordinates in LAMMPS," *Comput. Phys. Commun.*, vol. 190, pp. 120–128, 2015. DOI: [10.1016/j.cpc.2014.11.017](https://doi.org/10.1016/j.cpc.2014.11.017).
- [41] R. C. Raghu and J. Schofield, "Simulation of pressure-driven flows in nanochannels using multiparticle collision dynamics," *J. Phys. Chem. C*, vol. 114, no. 48, pp. 20659–20671, 2010. DOI: [10.1021/jp1055914](https://doi.org/10.1021/jp1055914).
- [42] B. Y. Cao, "Non-Maxwell slippage induced by surface roughness for microscale gas flow: A molecular dynamics simulation," *Mol. Phys.*, vol. 105, no. 10, pp. 1403–1410, 2007. DOI: [10.1080/00268970701361322](https://doi.org/10.1080/00268970701361322).

- [43] E. D. Miguel and G. Jackson, "The nature of the calculation of the pressure in molecular simulations of continuous models from volume perturbations," *J. Chem. Phys.*, vol. 125, no. 16, pp. 164109, 2006. DOI: [10.1063/1.2363381](https://doi.org/10.1063/1.2363381).
- [44] D. Han, et al., "Phonon thermal conduction in a graphene-C₃N heterobilayer using molecular dynamics simulations," *Nanotech.*, vol. 30, no. 7, pp. 075403, 2019. DOI: [10.1088/1361-6528/aaf481](https://doi.org/10.1088/1361-6528/aaf481).
- [45] X. Wang, J. Zhang, Y. Chen and P. K. Chan, "Investigation of interfacial thermal transport across graphene and an organic semiconductor using molecular dynamics simulations," *Phys. Chem. Chem. Phys.*, vol. 19, no. 24, pp. 15933–15941, 2017. DOI: [10.1039/C7CP01958K](https://doi.org/10.1039/C7CP01958K).
- [46] X. Wang, M. Wang, Y. Hong, Z. Wang and J. Zhang, "Coherent and incoherent phonon transport in a graphene and nitrogenated holey graphene superlattice," *Phys. Chem. Chem. Phys.*, vol. 19, no. 35, pp. 24240–24248, 2017. DOI: [10.1039/C7CP04219A](https://doi.org/10.1039/C7CP04219A).
- [47] X. Wang, J. Zhang, Y. Chen and P. K. Chan, "Molecular dynamics study of thermal transport in a dinaphtho[2,3-b:2',3'-f]thieno[3,2-b]thiophene (DNTT) organic semiconductor," *Nanoscale*, vol. 9, no. 6, pp. 2262–2271, 2017. DOI: [10.1039/c6nr08682a](https://doi.org/10.1039/c6nr08682a).
- [48] B. Li, J. Lan and L. Wang, "Interface thermal resistance between dissimilar anharmonic lattices," *Phys. Rev. Lett.*, vol. 95, no. 10, pp. 104302, 2005. DOI: [10.1103/PhysRevLett.95.104302](https://doi.org/10.1103/PhysRevLett.95.104302).
- [49] T. S. English, J. C. Duda, J. L. Smoyer, D. A. Jordan, P. M. Norris and L. V. Zhigilei, "Enhancing and tuning phonon transport at vibrationally mismatched solid-solid interfaces," *Phys. Rev. B*, vol. 85, no. 3, pp. 035438, 2012. DOI: [10.1103/PhysRevB.85.035438](https://doi.org/10.1103/PhysRevB.85.035438).
- [50] J. Sun and Z. X. Li, "Three-dimensional molecular dynamic study on accommodation coefficients in rough nanochannels," *Heat Transfer Eng.*, vol. 32, no. 7-8, pp. 658–666, 2011. DOI: [10.1080/01457632.2010.509759](https://doi.org/10.1080/01457632.2010.509759).
- [51] J. Sun and Z. X. Li, "Molecular dynamics simulations of energy accommodation coefficients for gas flows in nano-channels," *Mol. Simul.*, vol. 35, no. 3, pp. 228–233, 2009. DOI: [10.1080/08927020802395435](https://doi.org/10.1080/08927020802395435).
- [52] J. Sun and Z. X. Li, "Effect of gas adsorption on momentum accommodation coefficients in microgas flows using molecular dynamic simulations," *Mol. Phys.*, vol. 106, no. 19, pp. 2325–2332, 2008. DOI: [10.1080/00268970802452020](https://doi.org/10.1080/00268970802452020).
- [53] H. Yamaguchi, Y. Matsuda and T. Niimi, "Molecular-dynamics study on characteristics of energy and tangential momentum accommodation coefficients," *Phys. Rev. E*, vol. 96, no. 1, pp. 013116, 2017. DOI: [10.1103/PhysRevE.96.013116](https://doi.org/10.1103/PhysRevE.96.013116).
- [54] L. Li, J. Mo and Z. Li, "Flow and slip transition in nanochannels," *Phys. Rev. E*, vol. 90, no. 3, pp. 033003, 2014. DOI: [10.1103/PhysRevE.90.033003](https://doi.org/10.1103/PhysRevE.90.033003).
- [55] T. H. Chilton and A. P. Colburn, "Mass transfer (absorption) coefficients prediction from data on heat transfer and fluid friction," *Ind. Eng. Chem.*, vol. 26, no. 11, pp. 1183–1187, 1934. DOI: [10.1021/ie50299a012](https://doi.org/10.1021/ie50299a012).
- [56] A. P. Colburn, "A method of correlating forced convection heat-transfer data and a comparison with fluid friction," *Int. J. Heat Mass Transfer*, vol. 7, no. 12, pp. 1359–1384, 1964. DOI: [10.1016/0017-9310\(64\)90125-5](https://doi.org/10.1016/0017-9310(64)90125-5).
- [57] E. M. Sparrow and W. Q. Tao, "Symmetric vs asymmetric periodic disturbances at the walls of a heated flow passage," *Int. J. Heat Mass Transfer*, vol. 27, no. 11, pp. 2133–2144, 1984. DOI: [10.1016/0017-9310\(84\)90200-X](https://doi.org/10.1016/0017-9310(84)90200-X).
- [58] H.-Z. Huang and W. Q. Tao, "An experimental study on heat/mass transfer and pressure drop characteristics for arrays of nonuniform plate length positioned obliquely to the flow direction," *J. Heat Transfer*, vol. 115, no. 3, pp. 568–575, 1993. DOI: [10.1115/1.2910726](https://doi.org/10.1115/1.2910726).
- [59] S. S. Lue, H. Z. Huang and W. Q. Tao, "Experimental study on heat transfer and pressure drop characteristics in the developing region for arrays of obliquely positioned plates of nonuniform length," *Exp. Therm. Fluid Sci.*, vol. 7, no. 1, pp. 30–38, 1993. DOI: [10.1016/0894-1777\(93\)90078-W](https://doi.org/10.1016/0894-1777(93)90078-W).
- [60] Y. P. Cheng Z. G. Qu W. Q. Tao and Y. L. He, "Numerical design of efficient slotted fin surface based on the field synergy principle," *Numer. Heat Transfer, Part A*, vol. 45, no. 6, pp. 517–538, 2004.